Improved performance of electron cyclotron resonance heating by perpendicular injection in the Large Helical Device

Improved performance of electron cyclotron resonance heating by perpendicular injection in the Large Helical Device

T. Ii Tsujimura[1], R. Yanai[1], Y. Mizuno[1], K. Tanaka[1], Y. Yoshimura[1], T. Tokuzawa[1,2], M. Nishiura[1], R. Sakamoto[1,2], G. Motojima[1,2], S. Kubo[1], T. Shimozuma[1], H. Igami[1], H. Takahashi[1,2], M. Yoshinuma[1], S. Ohshima[3] and the LHD Experiment Group[1]

[1] National Institute for Fusion Science, National Institutes of Natural Sciences, Toki, Gifu 509-5292, Japan

[2] The Graduate University for Advanced Studies, SOKENDAI, Toki, Gifu 509-5292, Japan

[3] Institute for Advanced Energy, Kyoto University, Uji, Kyoto 611-0011, Japan

E-mail: `tsujimura.tohru@nifs.ac.jp`

23 October 2020

Abstract. A real-time interlock system for power injection in electron cyclotron resonance heating (ECRH) was developed to be applied to Large Helical Device (LHD) plasma. This system enabled perpendicular injection, thus improving the performance of ECRH more than ever achieved before in LHD. Perpendicular propagation of the electron cyclotron wave at 77 GHz became more insensitive to the effect of refraction in comparison to the conventional oblique propagation. The achieved central electron temperature in the case of perpendicular injection was approximately 2 keV higher than that in the case of standard oblique injection for a central electron density of 1×10^{19} m^{-3} by 1 MW injection. With such improved performance of ECRH, high-density ECRH plasma of 8×10^{19} m^{-3} was successfully sustained after the injection of multiple hydrogen ice pellets for the first time in LHD.

1. Introduction

In magnetically-confined fusion plasma, adjustments of launcher settings of electron cyclotron resonance heating (ECRH) are necessary to produce high-performance plasma, to realize desired power deposition profiles, to decrease the stray radiation level in the vessel, and to prevent damage of in-vessel components from unabsorbed power during high-power long-pulse injection. Single-pass absorption must be maximized to fulfill such requirements.

To obtain high single-pass absorption is strongly related to injection methods of ECRH. In the Large Helical Device (LHD), high-power gyrotrons have been introduced

to extend the operational regime of high central electron temperature (T_{e0}) and high central electron density (n_{e0}) [1]. This operational regime can be extended not only by the power increase of gyrotrons but also by adjustments of ECRH launcher settings. Perpendicular injection to the ECR layer is expected to be more insensitive to the effect of refraction. Historically, however, two kinds of injection methods of ECRH have been adopted in the current LHD experiments for their specific purposes: (i) injection from the upper port on the vertically-elongated plasma cross section (U-port injection) and (ii) injection from the outer port on the horizontally-elongated plasma cross section (O-port injection) [1, 2]. The U-port injection is suitable for plasma startup, but it is sensitive to refraction by high-n_e plasma. A 77-GHz gyrotron has been used for the U-port injection, which enables on-axis heating with the fundamental ordinary (O) mode in the standard magnetic configuration of LHD with a magnetic field strength of 2.75 T. The plasma cutoff density is 7.4×10^{19} m^{-3}. Even in $n_{e0} \sim 1 \times 10^{19}$ m^{-3}, the EC wave is easily refracted, so that tuning the launcher was performed with the ray-tracing code LHDGauss to obtain on-axis heating [3, 4]. The LHDGauss code runs on the AutoAna system [5], which is helpful for analyzing experimental data immediately after discharges on LHD. The fine tuning of launchers along with predictions of power deposition profiles by ray-tracing calculations contributed to the extension of the high-T regime [6]. However, the sensitivity to refraction prevents efficient heating in higher n_e. The cause of low heating performance is that the EC wave from the U port tangentially reaches the ECR layer. Most of the refracted wave cannot reach the ECR layer, which transmits over the plasma without absorption. The O-port injection improves the heating efficiency in high n_e in comparison to the U-port injection because the EC wave from the O-port injection can reach the ECR layer more perpendicularly. 77-GHz and 154-GHz gyrotrons have been used for the O-port injection. As shown in Fig. 1, the first walls are reinforced with molybdenum (Mo) on the opposite side of the launcher
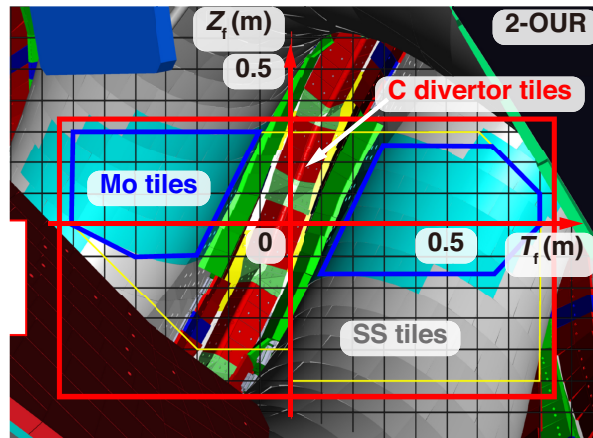

Figure 1. A drawing viewed from the center of the final mirror of the 2-OUR antenna (installed at the upper right side of the 2-O port) along with an imaginary target plane with a toroidally- and vertically-directed coordinate (T_f, Z_f) radially fixed at $R_f = 3.9$ m. First walls are reinforced with Mo on the opposite side of the launcher.

on the 2-O port. Thus, the standard injection method from the O port is oblique injection. Plasma startup can be also possible by the standard oblique injection. On the other hand, since the carbon divertor tiles on the opposite side of the launcher are fragile to transmitted high-power millimeter waves, perpendicular injection could not be applied in LHD before without an interlock system for power injection. Oblique injection contributes to EC current drive experiments as well [7]. Due to oblique propagation of the EC wave, however, the EC wave from the O-port injection is still sensitive to refraction in high n_e. The heating efficiency is observed to decrease gradually as n_e increases in the case of the standard oblique injection from the O port.

According to the current LHD project, there are strong needs for transport studies for isotope effects of high-n_e plasma with high-power ECRH. In contrast to 154-GHz ECRH, however, 77-GHz ECRH is rarely used for such transport studies at high n_e due to the effect of refraction [8, 9, 10, 11]. A real-time control system of the deposition location of ECRH was developed to mitigate the effect of refraction [12, 13]. The deposition location was adjusted according to time-varying n_e profiles. Higher absorption was successfully maintained longer due to the real-time deposition location control up to line-averaged density of $n_{e,avg} \sim 3 \times 10^{19}$ m^{-3}, where the deposition location was kept in the plasma core region. However, the absorption power decreased above 3×10^{19} m^{-3} even with the deposition location control. The effect of multi-pass absorption is expected to be dominant.

This situation has led to the necessity of perpendicular injection (i.e., perpendicular to the ECR layer) from the O port because it is expected to be more insensitive to the effect of refraction. The optical thickness for the fundamental O mode using 77 GHz increases as the propagation angle increases to reach 90°, i.e., perpendicular propagation [2]. Here, the optical thickness is calculated by the non-relativistic theory in a slab plasma [14, 15, 16]. Stronger absorption for the fundamental O mode with perpendicular propagation is expected. On the other hand, the fundamental extraordinary (X) mode is reflected at the right-hand cutoff layer located in front of the ECR layer. Although the unabsorbed transmitted wave propagates to the divertor region in LHD, as shown in Fig. 1, it is expected to be minute in principle. Figure 2 shows ray-tracing calculations in the cases of perpendicular injection and standard oblique injection for $n_{e,max} = 3 \times 10^{19}$ m^{-3}. The 77-GHz EC wave is launched from the 2-OUR antenna located at the upper right side of the 2-O port. Standard oblique injection is sensitive to refraction by the high-n_e plasma, which can decrease the first-pass absorption and achievable T_{e0}. On the other hand, perpendicular injection is more insensitive to the effect of refraction, which is verified with experiments and the results of improved heating performance are presented in the following sections of this paper. This perpendicular injection is a common similar heating method in tokamaks and the W7-X stellarator [17, 18]. For tokamaks, the magnetic field monotonically decreases with the major radius. Perpendicular injection from the low-field side on a poloidal plane was utilized in plasma startup and heating of tokamaks such as DIII-D [19], JT-60U [20], KSTAR [21], and TRIAM-1M [22]. However, for magnetic field
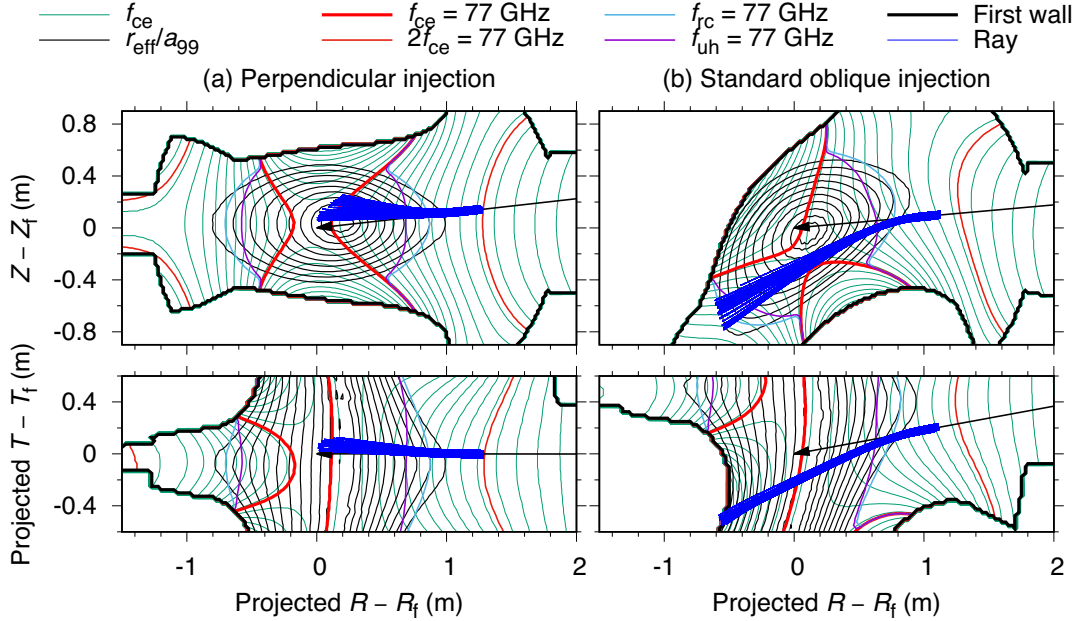
Figure 2. Ray-tracing calculations in the cases of (a) perpendicular injection and (b) standard oblique injection from the 2-OUR 77-GHz ECRH for $n_{e,max} = 3 \times 10^{19}$ m^{-3}. The rays are projected onto two planes: (top) the plane consisting of two orthogonal basis vectors, $\boldsymbol{e}_z \times (\boldsymbol{e}_z \times \boldsymbol{e}_{inj})$ and $\boldsymbol{e}_z$, and (bottom) the plane consisting of $\boldsymbol{e}_{tor} \times (\boldsymbol{e}_{tor} \times \boldsymbol{e}_{inj})$ and $\boldsymbol{e}_{tor}$, where $\boldsymbol{e}_z$, $\boldsymbol{e}_{tor}$, and $\boldsymbol{e}_{inj}$ denote the unit vector in the vertical direction, that in the toroidal direction at the 2-O port center, and that in the direction from the launching antenna mirror center to the target point. The arrowheads denote the target points. The contours of r_{eff}/a_{99} and the electron cyclotron frequencies f_{ce}, the lines of the right-hand cutoff frequency f_{rc}, the upper hybrid resonance frequency f_{uh}, and f_{ce} for 77 GHz, and the first walls are also superimposed on the planes. Here, r_{eff}/a_{99} denotes the effective minor radius normalized by the minor radius where 99% of the electron stored energy is confined. The target positions are set at $(R_f, T_f, Z_f) = (3.9, 0, 0)$ m for (a) and at $(R_f, T_f, Z_f) = (3.9, -0.5, 0.05)$ m for (b). The magnetic field strength is $B_t = 2.85$ T at the magnetic axis of $R_{ax} = 3.6$ m.

configurations such as LHD, the magnetic field is non-monotonic along the sight line due to the presence of the saddle point in the magnetic field isolines, as shown in Fig. 2, which makes the ray trajectories divergent and the deposition profile sensitive to the injection angle. Perpendicular injection will be also applicable to FFHR-c1, a candidate for helical DEMO reactors [23], along with the concept of a remote steering antenna [24], suitable for the blankets. When the 77-GHz EC wave is injected from the outside of the horizontally-elongated cross section, on-axis ECRH with perpendicular propagation is available only in the magnetic field increased with sub-cooled helical coils such as the magnetic field strength of $B_t = 2.85$ T at the magnetic axis of $R_{ax} = 3.6$ m [25]. In contrast to the fundamental O-mode heating with 77 GHz, 154-GHz EC waves for the second-harmonic X-mode heating were obliquely injected as usual from the O port for the experiments introduced in the following sections, because the effect of refraction is small in $n_e < 5 \times 10^{19}$ m^{-3}. In addition, a portion of the incident wave at 154 GHz

couples to the second-harmonic O-mode wave even when the incident polarization is controlled to excite the pure X mode in the actual experiments. The second-harmonic O-mode wave is in principle weakly absorbed, a part of which is transmitted to the divertor region through the plasma.

2. Effectiveness of perpendicular injection

The launching antenna 2-OUR for the fundamental O mode at 77 GHz was used to verify effectiveness of perpendicular injection in ECRH on LHD. Figure 1 shows a drawing viewed from the center of the final mirror of the 2-OUR antenna. In the drawing, an imaginary grid target plane is shown with a toroidally- and vertically-directed coordinate (T_f, Z_f) radially fixed at $R_f = 3.9$ m. The final mirror of the 2-OUR antenna is steerable, so that the target position can be changed toroidally and vertically. The target position was set at $(R_f, T_f, Z_f) = (3.9, -0.5, 0.05)$ m for standard oblique injection. The millimeter wave propagates into the first wall with Mo tiles under the vacuum condition. On the other hand, the target position was set at $(R_f, T_f, Z_f) = (3.9, 0, 0)$ m for perpendicular injection. Each target position for each injection was set so that the millimeter wave propagates to the magnetic axis on the vacuum magnetic surfaces, as shown in Fig. 2. The perpendicularly-injected millimeter wave propagates into the divertor region under the vacuum condition. The unabsorbed transmitted EC wave can reach the divertor region when the O mode is less absorbed under considerably low n_e. Thus, ECRH with perpendicular injection cannot be used for plasma startup in LHD. Plasma must be sustained by other ECRH with oblique injection from the O port. In order to prevent the unfavorable damage of the divertor region by the transmitted wave, the interlock system for the power output from the gyrotron was developed. The interlock system constructed was based on the same system as real-time deposition location control of ECRH [12, 13]. This system was controlled with real-time FPGA (field programmable gate array) processing on a CompactRIO made by National Instruments. For details, refer to the previous work [12, 13]. The real-time acquisition was performed for $n_{e,avg}$ measured with the FIR laser interferometer and one-channel T_e measured with the EC emission (ECE) diagnostic [26, 27]. The appropriate threshold settings for the parameters guaranteed that confined plasma was maintained and perpendicular injection could be available.

With the system, the interlock for power injection only to plasma of $n_{e,avg} > 0.5 \times 10^{19}$ m^{-3} sustained by other ECRH functioned correctly to produce no unfavorable sparks from the divertor region. Figure 3 shows a typical discharge of modulation ECRH experiments to evaluate the heating performance. The plasma was sustained by two 154-GHz gyrotrons. Then, the power of 2-OUR 77-GHz ECRH was modulated at 11 Hz and was perpendicularly injected from the O port. The time evolution of T_e was measured with the Thomson scattering diagnostic [28]. As shown in Fig. 3(c), higher modulated T_e in the case of perpendicular injection was observed than that in the case of standard oblique injection. The measured point $R = 3.646$ m is close to the
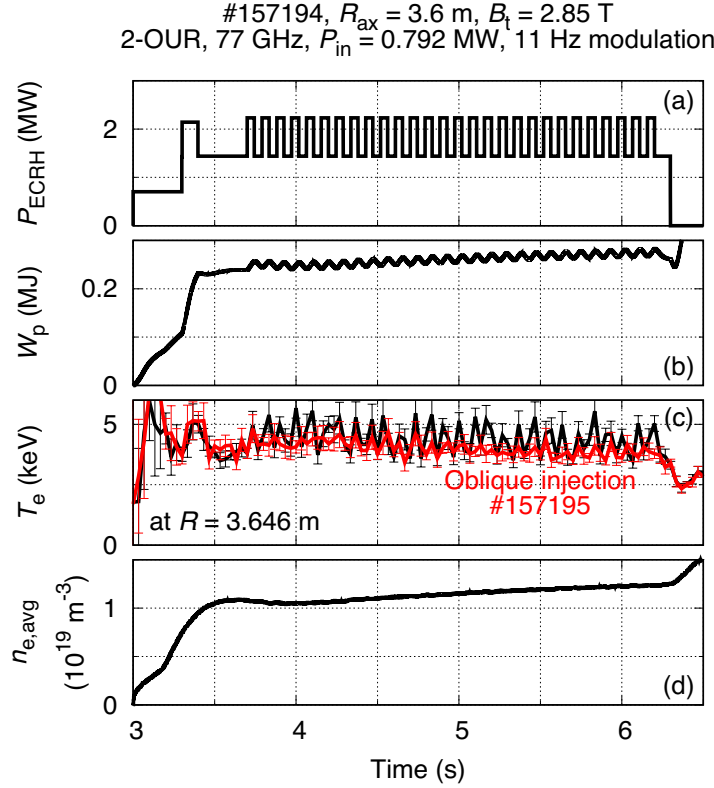
Figure 3. Time evolution of (a) injection power of ECRH, (b) the plasma stored energy W_p, (c) electron temperature T_e at $R = 3.646$ m, and (d) $n_{e,avg}$ in the case of perpendicular injection. T_e in the case of oblique injection is also plotted for comparison.

magnetic axis. In order to evaluate the radial profile of modulated T_e components, the conditional-averaging technique was applied to the Thomson scattering data during the modulation ECRH [29]. The analysis was performed in the stationary period during modulation, where $n_{e,avg}$ and the plasma stored energy W_p were almost constant. Figures 4(a) and (b) show comparisons of the T_e responses between perpendicular injection and oblique injection in modulation ECRH. The perturbation amplitude of T_{e0} in the case of perpendicular injection was higher than that in the case of oblique injection. Perpendicular injection shows better central heating than oblique injection, although the absorption power was almost the same in both cases as shown in Fig. 6(c). Figures 4(c) and (d) show the power spectral density (PSD) and the phase delay of modulated T_e signals measured with the ECE diagnostic. The amplitude peak and the phase bottom could not be recognized in the case of $n_{e,avg} \simeq 1 \times 10^{19}$ m^{-3} due to the lack of ECE channels near the magnetic axis. On the other hand, the amplitude peak and the phase bottom could be recognized at $r_{eff}/a_{99} \sim 0.7$ in the case of $n_{e,avg} \simeq 2 \times 10^{19}$ m^{-3} and oblique injection. This suggests that the deposition shifted outward. Refraction and Doppler-shifted absorption in oblique propagation of the EC wave caused broadening of the deposition profile, in particular, at higher n_e. This effect could not be compensated with the real-time deposition location control in high n_e, which could only change the
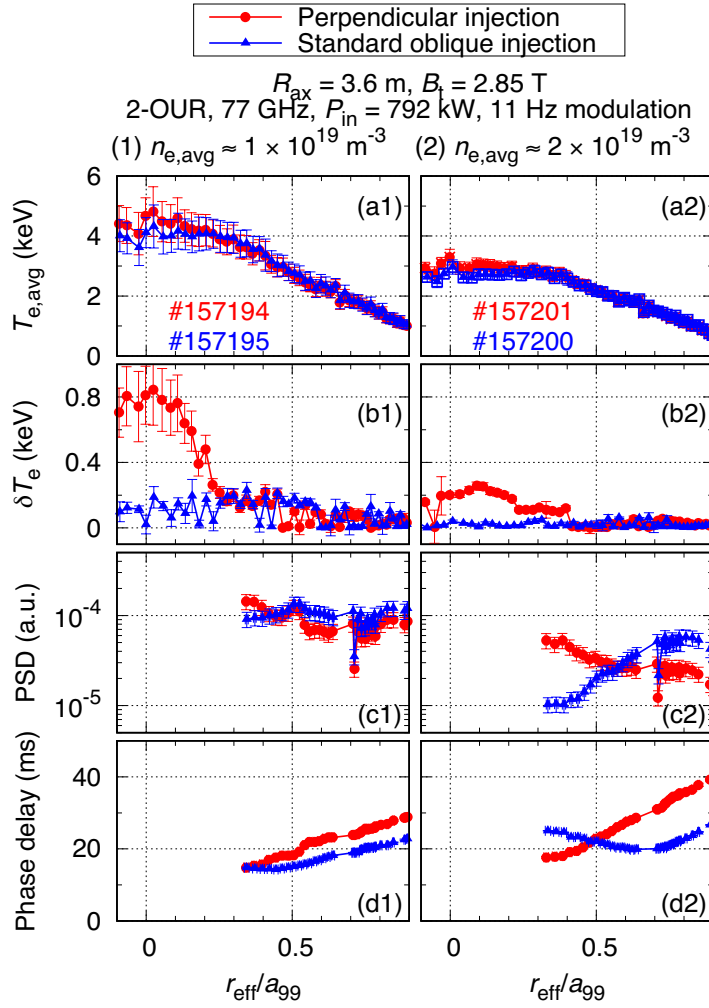
Figure 4. Comparisons of radial profiles of (a) conditional-averaged T_e and (b) its perturbation δT_e measured with the Thomson scattering diagnostic and (c) the power spectral density (PSD) and (d) the phase delay of modulated T_e signals measured with the ECE diagnostic at the modulation frequency of 11 Hz in the cases of (1) $n_{e,avg} \simeq 1 \times 10^{19}$ m^{-3} and (2) $n_{e,avg} \simeq 2 \times 10^{19}$ m^{-3}.

deposition peak location. The deposition width could not be controlled. These results clearly demonstrated that perpendicular injection is more insensitive to refraction and Doppler effects than oblique injection, as expected. Ray-tracing calculations by the LHDGauss code, as shown in Fig. 5, also show better central heating in the case of perpendicular injection and broader deposition in the case of oblique injection. Influence of high energy electrons on power depositions can be negligible in $n_{,avg} \gtrsim 1 \times 10^{19}$ m^{-3} [30]. Density scan in 1×10^{19} m$^{-3} < n_{e,avg} < 4 \times 10^{19}$ m^{-3} was performed in modulation ECRH experiments, as shown in Fig. 6. The perturbation amplitude of T_e averaged inside $r_{eff} = 0.1$ m decreased as $n_{e,avg}$ increased even in the case of perpendicular injection due to the effect of refraction. However, the absorption power in the case of perpendicular injection was maintained higher than that in the case of oblique injection for high density of $n_{e,avg} > 3 \times 10^{19}$ m^{-3}. Better heating efficiency by
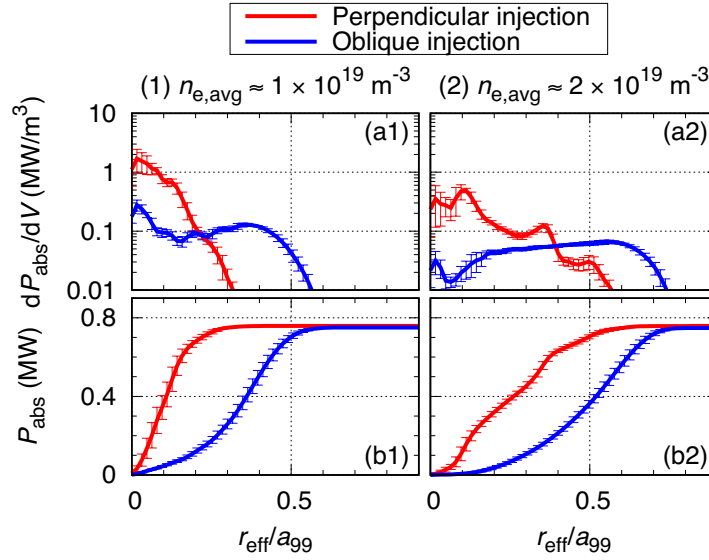
Figure 5. Comparisons of radial profiles of (a) power deposition dP_{abs}/dV and (b) integrated absorbed power P_{abs} calculated by the LHDGauss code for the discharges shown in Fig. 4.

perpendicular injection can contribute to transport studies in $n_{\text{e}} < 5 \times 10^{19}$ m^{-3} by gas puffing [9, 10, 11].

In order to maximize single-pass absorption, optimization of the incident EC wave polarization is important because the O-X mode coupling is affected by the strong magnetic shear and the finite plasma density at the peripheral region in LHD [31]. Polarization scan experiments were performed for relatively low-n_{e} plasma. Figure 7 shows the results on absorption power as a function of polarization states. A polarization state is represented by (α, β), where α and β denote the rotation angle and the ellipticity of the polarization ellipse. $\alpha = 0°$ is defined as the toroidal direction [3]. The incident millimeter wave couples to the EC waves with the O mode and the X mode under their orthogonality. In this heating scenario, the pure O mode has to be excited to maximize the single-pass absorption. The X mode is reflected at the right-hand cutoff layer in front of the ECR layer, which causes the increase in multi-pass absorption. Each mode purity η_σ is represented by

$$\eta_\sigma = \cos^2(\alpha - \alpha_\sigma)\cos^2(\beta - \beta_\sigma) + \sin^2(\alpha - \alpha_\sigma)\sin^2(\beta + \beta_\sigma), \ \sigma = \text{O, X},$$

where $(\alpha_\sigma, \beta_\sigma)$ is the optimum polarization state to excite each mode [3]. Then, the experimental data were fitted using the above equation, as shown in Fig. 7. These results show that the linear polarization of $(\alpha, \beta) \simeq (45°, 0°)$ is optimum to excite the pure O mode in low-n_{e} plasma of $\sim 1.5 \times 10^{19}$ m^{-3}. The multi-pass absorption component is estimated to be 0.3 at the polarization state of $(\alpha, \beta) \simeq (-45°, 0°)$, which is optimum to excite the pure X mode for the first path but relates to the stray radiation level in the vessel. The optimum polarization states for each mode are also confirmed from the mode content analysis using the LHDGauss code [3].
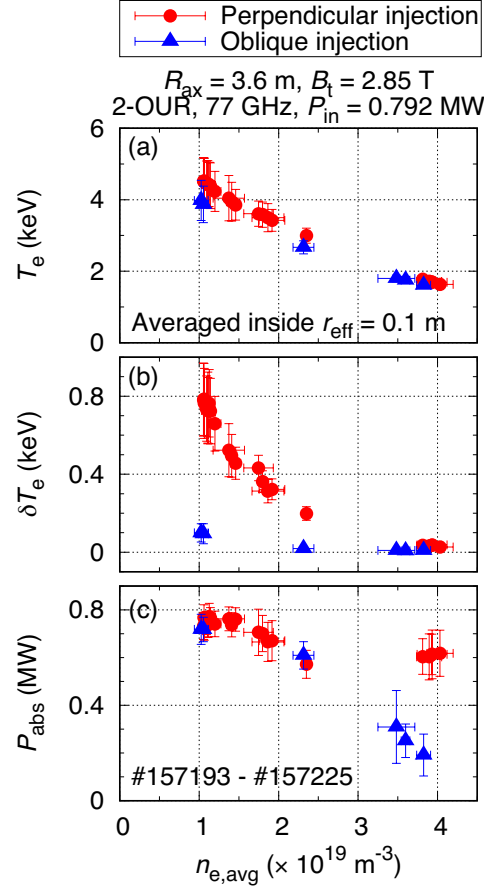
Figure 6. Comparisons of (a) conditional-averaged T_e and (b) its perturbation δT_e averaged inside $r_{eff} = 0.1$ m and (c) absorption power P_{abs} as a function of $n_{e,avg}$. P_{abs} was experimentally evaluated from the response of the plasma stored energy to the power modulation of 11 Hz.

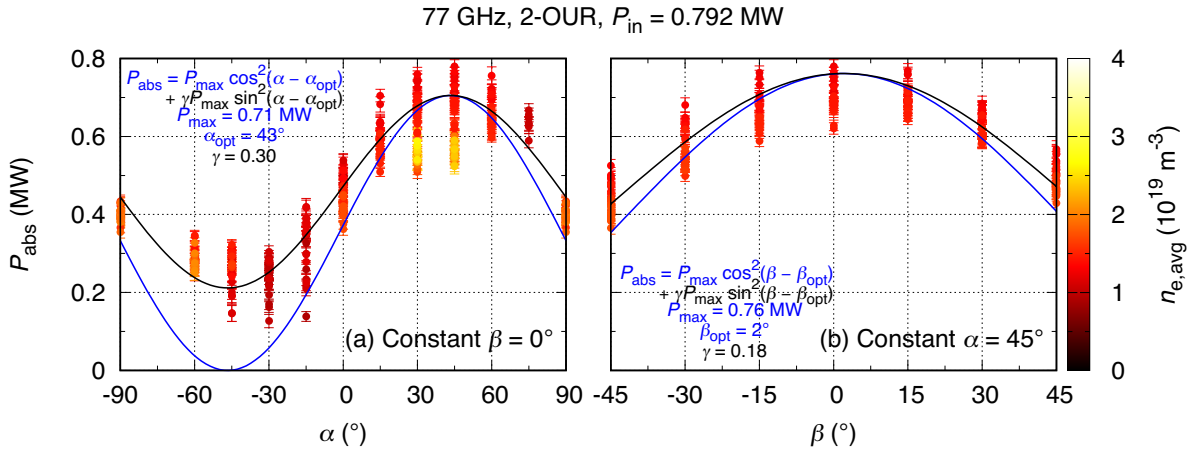**Figure 7.** Absorption power P_{abs} as a function of (a) the polarization rotation angle α and (b) the ellipticity β of the incident EC wave injected perpendicularly. Profiles fitted to the experimental data are also plotted.

3. Improved performance of ECRH

Effectiveness of perpendicular injection for 77 GHz is verified in the previous section. With the improved performance of ECRH, achieved T_e profiles were compared between the two kinds of injection of 1 MW without modulation. Plasma was sustained by two 154-GHz gyrotrons with 1 MW injection power each. As shown in Fig. 8, T_{e0} increased from 4 keV to over 6 keV by perpendicular injection for $n_{e,avg} \simeq 1 \times 10^{19}$ m^{-3}. The achieved T_{e0} was approximately 2 keV higher than that in the case of oblique injection because the calculated deposition profile for oblique injection is broader, as shown in Fig. 9. The better central heating performance by perpendicular injection will contribute to extending the high-temperature regime in LHD [6].

Such an improved ECRH performance using perpendicular injection has opened up a new operational region in LHD ECRH plasma with hydrogen ice pellet injection [32]. In these experiments, plasma was sustained by two 154-GHz gyrotrons and one 77-GHz gyrotron. The 77-GHz EC wave was injected perpendicularly or obliquely for comparison. As shown in Fig. 10 for the case of perpendicular injection, high-n_e ECRH plasma of $n_{e0} \sim 8 \times 10^{19}$ m^{-3} was successfully sustained after injection of three consecutive hydrogen ice pellets for the first time in LHD. Hollow n_e profiles by gas puffing changed to rather peaked profiles after the pellet injection. Equipartition heating was significant in the high-n_e region: $T_{i0} \sim T_{e0} \sim 1$ keV were obtained. On the other hand, in the case of oblique injection, the high-n_e plasma was radiatively collapsed after the pellet injection due to the decreased absorption power. The difference of heating
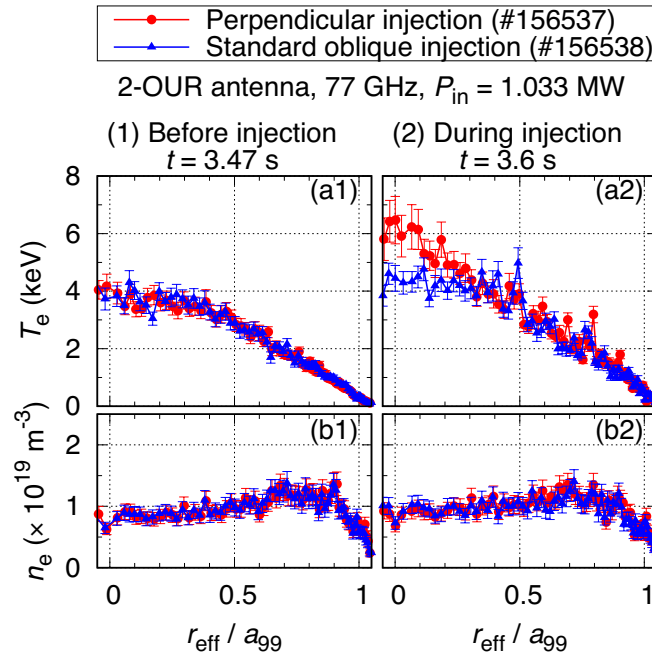

Figure 8. Comparisons of radial profiles of (a) T_e and (b) n_e (1) before and (2) during perpendicular/oblique injection.
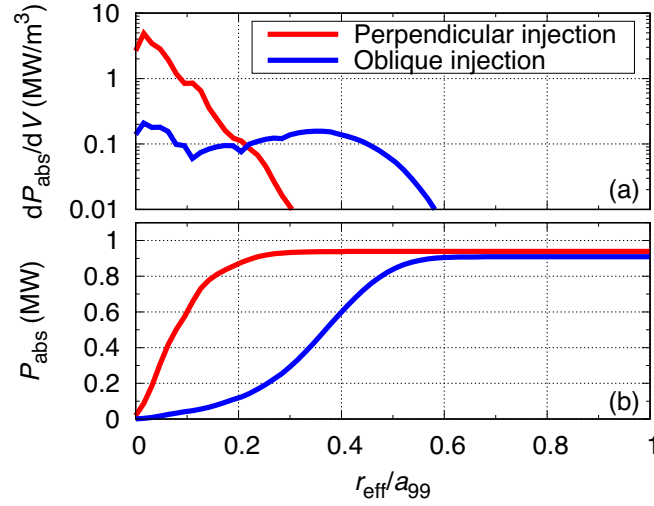
Figure 9. Comparisons of radial profiles of (a) power deposition dP_{abs}/dV and (b) integrated absorbed power P_{abs} calculated by the LHDGauss code for the discharges shown in Fig. 8.
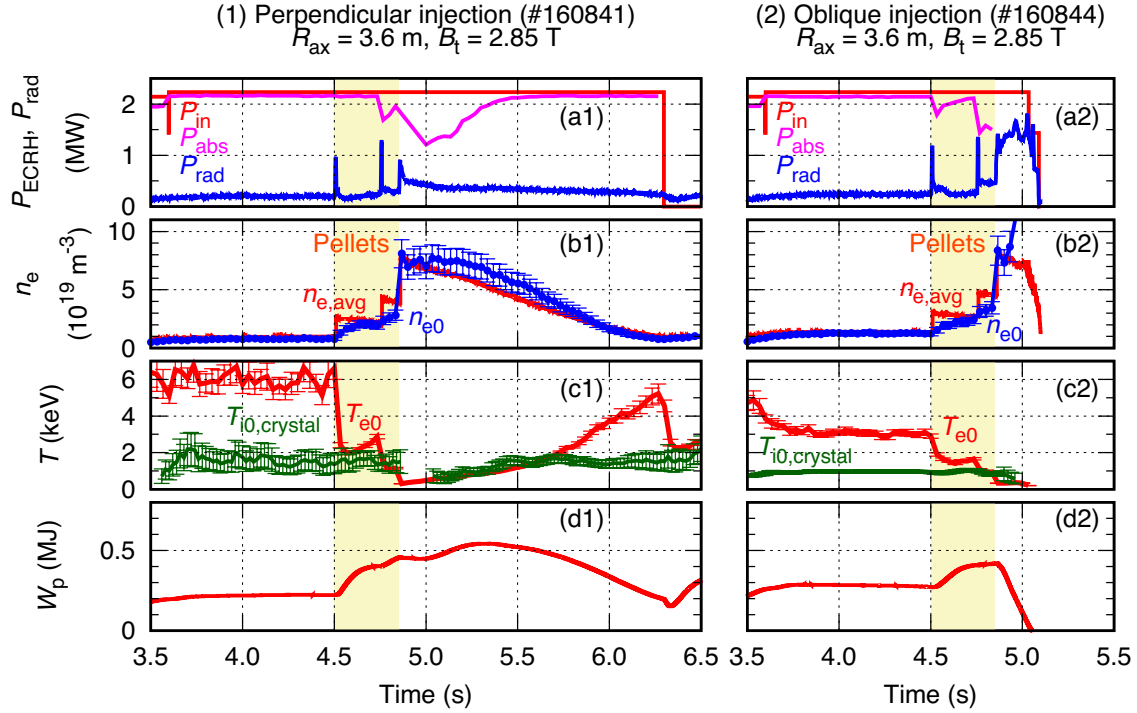

Figure 10. Comparisons of time evolution of (a) injection power P_{in} and absorption power P_{abs} of ECRH, radiation power P_{rad}, (b) $n_{e,avg}$, n_{e0}, (c) T_{e0}, T_{i0} measured with the crystal spectrometer, and (d) W_p between (1) perpendicular injection and (2) oblique injection.

performance was confirmed in the H_α emission from the ablating pellets as shown in Fig. 11, which indicates the penetration depth of each pellet. The penetration depth depends mainly on T_e. Since T_{e0} in the case of oblique injection was lower than that
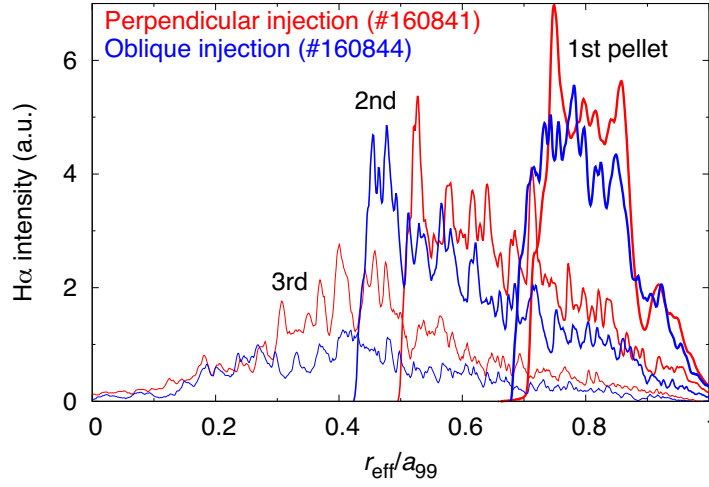
Figure 11. Comparison of radial profiles of H_α intensity between perpendicular injection and oblique injection during pellet injection for the discharges shown in Fig. 10.

in the case of perpendicular injection, the penetration depth in the case of oblique injection was deeper than that in the case of perpendicular injection especially for the second pellet injection. The better fueling efficiency and the decreased heating power by oblique injection caused the increased n_{e0} and the radiative collapse.

The new launch scheme which makes possible an operation with high-n_e in ECRH plasma will promote comparative studies between devices. High-n_e ECRH plasma with $T_{e0} \sim T_{i0}$ was compared with W7-X high-n_e plasma for a reference to Fig. 2 of [33]. Figure 12 shows an example of a typical discharge of high-n_e ECRH plasma using multiple pellet injection. When W_p reached a plateau at around 4.1 s, the plasma parameters were the following: $P_{in,ECRH} = 2.79$ MW, $n_{e0} \sim 7.5 \times 10^{19}$ m^{-3}, $T_{i0} \sim 1$ keV, $W_p \sim 0.6$ MJ, the energy confinement time $\tau_E \sim 0.22$ s, and the fusion triple product $n_{e0}\tau_E T_{i0} \sim 1.6 \times 10^{19}$ m^{-3} s keV, which resulted in $(\sim 1/2) P_{in,ECRH}$, $(\sim 1) n_{e0}$, $(\sim 1/3) T_{i0}$, $(\sim 1/2) W_p$, $(\sim 1) \tau_E$, and $(\sim 1/4) n_{e0}\tau_E T_{i0}$ of the W7-X reference discharge. Accumulating a database of discharges with a wide range of heating power and electron density will accelerate comparative studies in confinement and transport between different devices.

The new launch scheme which makes possible an operation with high-n_e in ECRH plasma will also promote isotope effect studies in LHD. Figure 13 shows an example of comparisons with the international stellarator scaling, ISS04 [34], in hydrogen plasma and deuterium plasma. Here, in the hydrogen case, the plasma was started up with hydrogen gas puffing followed by injection of three consecutive hydrogen ice pellets. In the deuterium case, the plasma was started up with deuterium gas puffing followed by injection of three consecutive deuterium ice pellets. Dependence of W_p on $n_{e,avg}$ is shown. W_p is normalized by $P_{in,ECRH}^{0.39}$, whose exponent is based on the scaling [34]. The low-n_e hydrogen plasma during gas puffing before pellet injection located almost along the scaling. Then, the plasma behaved adiabatically during the first pellet injection
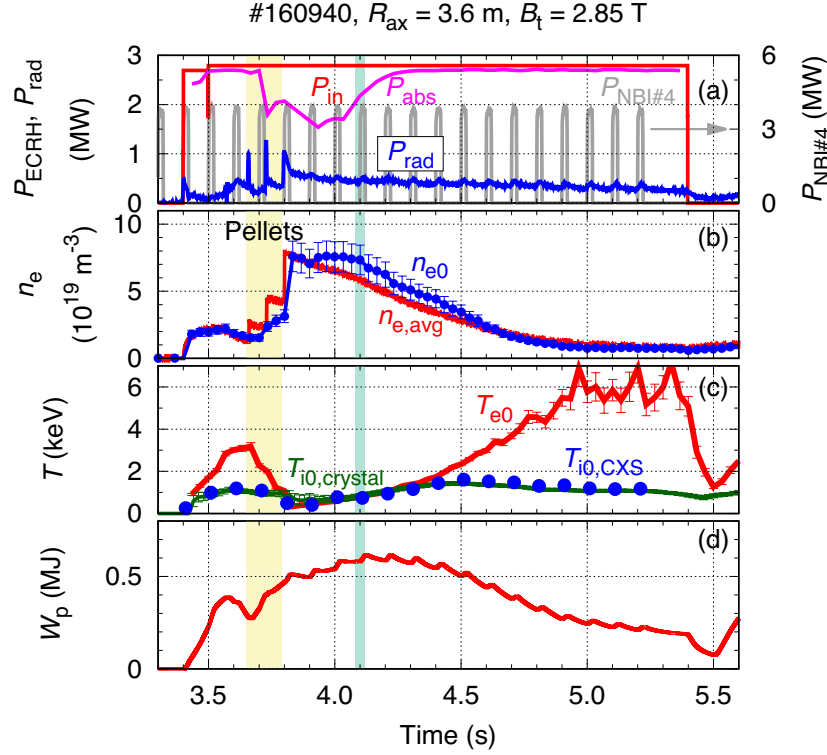
Figure 12. Time evolution of (a) $P_{\rm in}$ and $P_{\rm abs}$ of ECRH, $P_{\rm rad}$, port-through power of NBI#4 for $T_{\rm i}$ measurements, (b) $n_{\rm e,avg}$, $n_{\rm e0}$, (c) $T_{\rm e0}$, $T_{\rm i0}$ measured with the crystal spectrometer, $T_{\rm i0}$ measured with the charge exchange spectroscopy, and (d) $W_{\rm p}$.
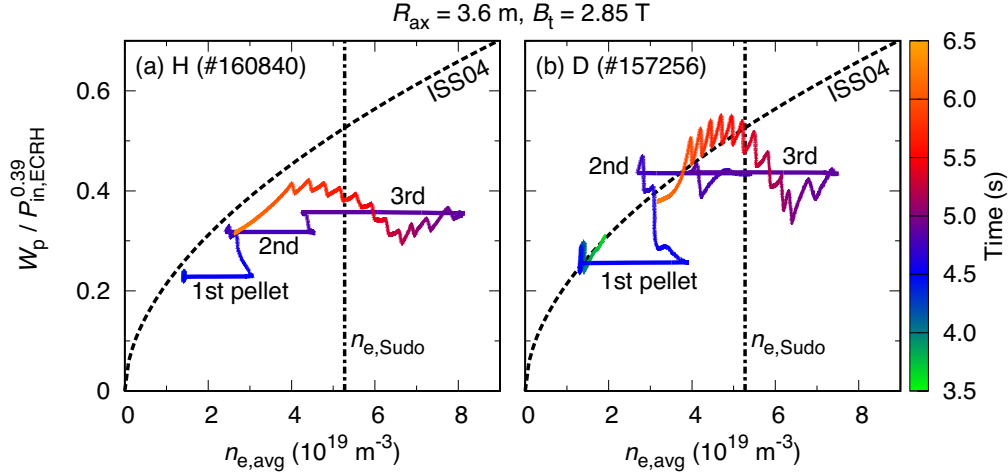

Figure 13. Comparisons with the ISS04 scaling in (a) hydrogen plasma and (b) deuterium plasma sustained with multiple pellet injection. $W_{\rm p}$ normalized by $P_{\rm in}^{0.39}$ of ECRH is plotted as a function of $n_{\rm e,avg}$. Here, $a_{99} = 0.63$ m and $\iota_{2/3} = 0.65$ are assumed [34], where $\iota_{2/3}$ denotes the rotational transform at $r_{\rm eff}/a_{99} = 2/3$.

and then relaxed to the state almost along the scaling after the pellet. The plasma transiently exceeded the Sudo density limit [35] after the third pellet injection while the plasma relaxed to the state relatively beneath the scaling. In contrast, the normalized

$W_{\rm p}$ in the deuterium plasma was relatively larger than that in the hydrogen plasma after the third pellet injection although the injection power of ECRH was the same between the two discharges. The deuterium plasma relaxed to the state almost along the scaling even in high $n_{\rm e}$. The confinement properties depending on the isotope mass cannot be concluded yet only with this example. Isotope effects on energy, particle transport and turbulence have been discussed in relatively low-$n_{\rm e}$ ECRH plasma with gas puffing [10, 11]. Experiment data in a wide range of $n_{\rm e}$ and ECRH power will be accumulated in order to discuss the isotope effect in high-$n_{\rm e}$ ECRH plasma with pellet injection as a future work.

4. Summary and outlook

A method of perpendicular injection from the O port was developed in order for the EC wave to be more insensitive to the effect of refraction in LHD. The achieved $T_{\rm e0}$ in the case of perpendicular injection was approximately 2 keV higher than that in the case of oblique injection for $n_{\rm e0} \sim 1 \times 10^{19}$ m^{-3} by 1 MW injection. With such an improved performance of ECRH, high-density ECRH plasma of $n_{\rm e0} \sim 8 \times 10^{19}$ m^{-3} was successfully sustained after multiple hydrogen pellet injections. This method as well as the real-time deposition location control for efficient first-pass absorption in the plasma core region are beneficial not only for preventing damage of in-vessel components during long-pulse operations but also for extending high-temperature operational regimes and conducting precise transport studies.

For a future outlook, further improvement of ECRH performance up to plasma cutoff density is envisaged by proposing the fundamental O-mode perpendicular injection on the vertically-elongated cross section in LHD. Figure 14 shows comparisons of ray trajectories for four different injection methods in $n_{\rm e0} = 7 \times 10^{19}$ m^{-3}. The calculations were performed with the TRAVIS code [36], whose specially designed graphical user interface (GUI) is easy to use in order to study and design the new launch scheme by graphically changing the launching angle, the launching position, or plasma parameters. The newly-proposed perpendicular injection shown in Fig. 14(d) can be efficient in heating up to the plasma cutoff density of 7.4×10^{19} m^{-3} because the propagation path is shorter than that in the case of perpendicular injection from the O port on the horizontally-elongated cross section, whose heating performance is presented in this paper. Peripheral heating by the obliquely-injected X mode can be also expected up to the left-hand cutoff density if the final mirror is steerable. The launched millimeter wave from corrugated waveguides at a U port should be reflected at the final mirror installed outside on the equatorial plane of the vertically-elongated cross section. A feasible launcher is under development.
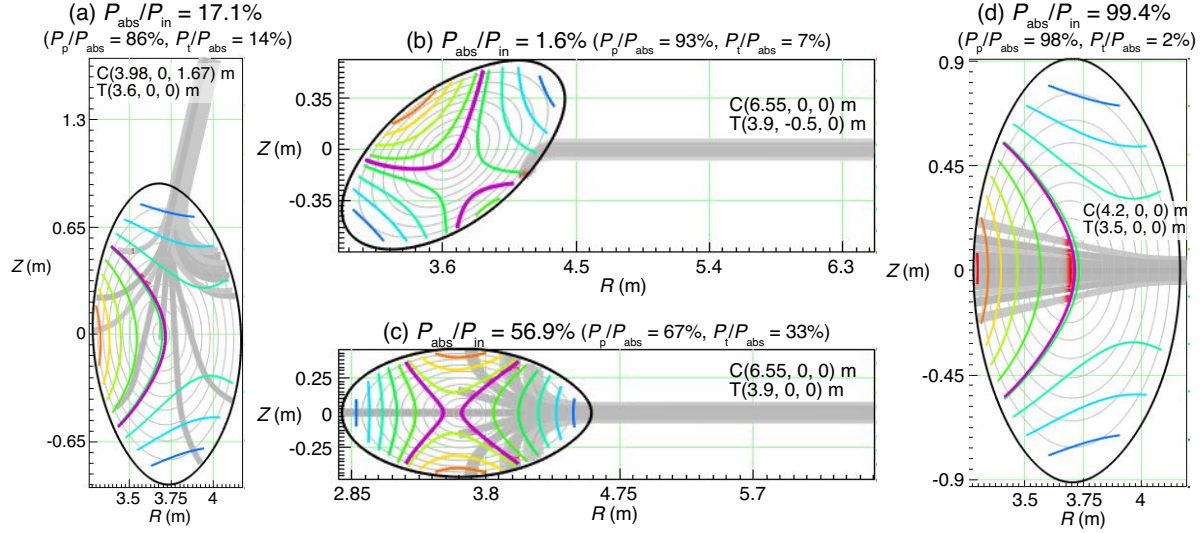
Figure 14. Ray trajectories of the fundamental O mode for (a) the conventional U-port injection, (b) the conventional O-port oblique injection, (c) the O-port perpendicular injection on the horizontally-elongated cross section, and (d) the U-port perpendicular injection on the vertically-elongated cross section. Magnetic surfaces and isolines of magnetic field strength are also shown. The resonance line at $B = 2.75$ T is shown in thick violet lines. The center of each final mirror and the target position are shown by C(R, T, Z) and T(R, T, Z), respectively. The incident millimeter wave is represented by a cylinder with a radius of 50 mm at the electric field strength of $1/e$. The magnetic field configuration is $R_{ax} = 3.6$ m, $B_t = 2.81$ T, and the plasma beta $\beta = 0.44\%$. Profiles of n_e and T_e are given by $n_e = n_{e0}(1 - \rho^8)$ and $T_e = T_{e0}[0.8 + 0.2(1 - \rho^4)^{1.1} - 0.7(1 - e^{-(\rho/0.5)^2})]$, where $\rho = r_{eff}/a_{99}$, $n_{e0} = 7 \times 10^{19}$ m^{-3}, and $T_{e0} = 2.5$ keV. The absorption power P_{abs} is normalized by the injection power P_{in}. The contributions to P_{abs} from passing electrons (P_p) and trapped electrons P_t are evaluated.

Acknowledgments

References

[1] Takahashi H. *et al* 2014 Extension of high T_e regime with upgraded electron cyclotron resonance heating system in the Large Helical Device *Phys. Plasmas* **21** 061506
[2] Shimozuma T. *et al* 2015 Optimization of the high harmonic ECRH scenario to extend a heating plasma parameter range in LHD *Nucl. Fusion* **55** 063035
[3] Ii Tsujimura T. *et al* 2015 Development and application of a ray-tracing code integrating with 3D equilibrium mapping in LHD ECH experiments *Nucl. Fusion* **55** 123019
[4] Tsujimura T. I. *et al* 2016 Impact of the LHD Peripheral Region and the Magnetic Axis Shift on Optimal On-Axis ECRH Injection for High-Electron-Temperature Plasmas *Preprint: 2016 IAEA Fusion Energy Conf. (Kyoto, Japan)* IAEA-CN-234-0083

[5] Emoto M. *et al* 2014 Automatically processing physical data from LHD experiments *Fusion Eng. Des.* **89** 758

[6] Takahashi H. *et al* 2017 Extension of operational regime in high-temperature plasmas and effect of ECRH on ion thermal transport in the LHD *Nucl. Fusion* **57** 086029

[7] Yoshimura Y. *et al* 2016 Improvement in Flexibility of ECCD by Upgraded ECH Antenna System on LHD *Plasma Fusion Res.* **11** 2402036

[8] Kobayashi T. *et al* 2018 Density dependence of transient electron thermal transport property in LHD *Nucl. Fusion* **58** 126031

[9] Warmer F. *et al* 2018 Energy confinement of hydrogen and deuterium electron-root plasmas in the Large Helical Device *Nucl. Fusion* **58** 106025

[10] Tanaka K. *et al* 2019 Isotope effects on energy, particle transport and turbulence in electron cyclotron resonant heating plasma of the Large Helical Device *Nucl. Fusion* **59** 126040

[11] Tanaka K. *et al* 2020 Extended investigations of isotope effects on ECRH plasma in LHD *Plasma Phys. Control. Fusion* **62** 024006

[12] Ii Tsujimura T. *et al* 2020 Real-time control of the deposition location of ECRH in the LHD *Fusion Eng. Des.* **153** 111480

[13] Ii Tsujimura T. *et al* 2018 Real-time control of electron cyclotron wave polarization in the LHD *Fusion Eng. Des.* **131** 130

[14] England A. C, Eldridge O. C, Knowlton S. F., Porkolab M. and Wilson J. R. 1989 Power transmission and coupling for radiofrequency heating of plasmas *Nucl. Fusion* **29** 1527

[15] Litvak A. G., Permitin G. V., Suvorov E. V. and Frajman A. A. 1977 Electron-cyclotron heating of plasma in toroidal systems *Nucl. Fusion* **17** 659

[16] Bornatici M. 1982 Theory of electron cyclotron absorption of magnetized plasmas *Plasma Physics* **24** 629

[17] Erckmann V. *et al* 2007 Electron Cyclotron Heating for W7-X: Physics and Technology *Fusion Sci. Technol.* **52** 291

[18] Stange T. *et al* 2017 Advanced electron cyclotron heating and current drive experiments on the stellarator Wendelstein 7-X *EPJ Web Conf.* **157** 02008

[19] Jackson G. L., deGrassie J. S., Moeller C. P. and Prater R. 2007 Second harmonic electron cyclotron pre-ionization in the DIII-D tokamak *Nucl. Fusion* **47** 257

[20] Kajiwara K. *et al* 2005 Electron cyclotron heating assisted startup in JT-60U *Nucl. Fusion* **45** 694

[21] Bae Y. S. *et al* 2009 ECH pre-ionization and assisted startup in the fully superconducting KSTAR tokamak using second harmonic *Nucl. Fusion* **49** 022001

[22] Idei H. *et al* 2006 Electron cyclotron current drive experiments in LHCD plasmas using a remote steering antenna on the TRIAM-1M tokamak *Nucl. Fusion* **46** 489

[23] Miyazawa J. *et al* 2017 Conceptual design of a liquid metal limiter/divertor system for the FFHR-d1 *Fusion Eng. Des.* **125** 227

[24] Kasparek W. *et al* 2003 Performance of a remote steering antenna for ECRH/ECCD applications in ITER using a four-wall corrugated square waveguide *Nucl. Fusion* **43** 1505

[25] Hamaguchi S., Imagawa S., Obana T., Yanagi N. and Mito T. 2018 Operations of the Helium Subcooling System for the LHD Helical Coils during Ten Plasma Experimental Campaigns *Plasma Fusion Res.* **13** 3405057

[26] Akiyama T. *et al* 2010 Interferometer Systems on LHD *Fusion Sci. Technol.* **58** 352

[27] Tsuchiya H., Nagayama Y., Kawahata K., Inagaki S., Kubo S. and LHD Experiment Group 2011 Design and Installation of a New Electron Cyclotron Emission Diagnostic Antenna in LHD *Plasma Fusion Res.* **6** 2402114

[28] Yamada I. *et al* 2016 Calibrations of the LHD Thomson scattering system *Rev. Sci. Instrum.* **87** 11E531

[29] Kobayashi T. *et al* 2016 Reconstruction of high temporal resolution Thomson scattering data during a modulated electron cyclotron resonance heating using conditional averaging *Rev. Sci. Instrum.* **87** 043505

[30] Kubo S. *et al* 2012 Influence of high energy electrons on ECRH in LHD *EPJ Web Conf.* **32** 02007

[31] Tsujimura T. I. *et al* 2016 Optimization of Incident EC Wave Polarization in Real-Time Polarization Scan Experiments on LHD *Plasma Fusion Res.* **11** 2402016

[32] Sakamoto R. *et al* 2013 Twenty barrel *in situ* pipe gun type solid hydrogen pellet injector for the Large Helical Device *Rev. Sci. Instrum.* **84** 083504

[33] Bozhenkov S. A. *et al* 2020 High-performance plasmas after pellet injections in Wendelstein 7-X *Nucl. Fusion* **60** 066011

[34] Yamada H. *et al* 2005 Characterization of energy confinement in net-current free plasmas using the extended International Stellarator Database *Nucl. Fusion* **45** 1684

[35] Sudo S., Takeiri Y., Zushi H., Sano F., Itoh K., Kondo K. and Iiyoshi A. 1990 Scalings of energy confinement and density limit in stellarator/heliotron devices *Nucl. Fusion* **30** 11

[36] Marushchenko N. B., Turkin Y. and Maassberg H 2014 Ray-tracing code TRAVIS for ECR heating, EC current drive and ECE diagnostic *Comput. Phys. Commun.* **185** 165